

Time-domain Reflectometry (TDR) technique for the estimation of soil permittivity

Original

Time-domain Reflectometry (TDR) technique for the estimation of soil permittivity / Savi, Patrizia; S., Ferraris; Maio, Ivano Adolfo - In: Principles, Application and Assessment in Soil Science / Prof. Dr. E. Burcu Ozkaraova Gungor. - Rijeka : INTECH, 2011. - ISBN 9799533072752. - pp. 351-370

Availability:

This version is available at: 11583/2460878 since:

Publisher:

INTECH

Published

DOI:

Terms of use:

This article is made available under terms and conditions as specified in the corresponding bibliographic description in the repository

Publisher copyright

(Article begins on next page)

Time-Domain Reflectometry (TDR) Technique for the Estimation of Soil Permittivity

Patrizia Savi¹, Ivan A. Maio¹ and Stefano Ferraris²

¹*Dipartimento di Elettronica, Politecnico di Torino,
C.so Duca degli Abruzzi 24, 10129 Torino*

²*Università degli Studi di Torino, Dipartimento di Economia e Ingegneria Agraria,
Forestale e Ambientale (D.E.I.A.F.A.), Sezione di Idraulica Agraria,
Via Leonardo da Vinci 44, 10095 Grugliasco, Torino
Italy*

1. Introduction

Time Domain Reflectometry (TDR) has been initially developed as a remote sensing electrical measurement tool and it has been widely used to detect cable faults and discontinuities of signal lines (Somlo & Hollway, 1969). Recently, TDR has been widely applied to soil science, hydrology and agronomy to estimate the electrical properties of soils (Courtney, 1998; Evett & Parkin, 2005; Nozaki & Bose, 1990; Robinson et al., 2003; Topp & Ferre', 2002).

The two major features of TDR waveforms are the travel time and the response 'late' time amplitude: they are directly related to the apparent dielectric constant K_a and to the soil electrical conductivity γ (Robinson et al., 2005). If the assumption is made that the imaginary part of the complex electrical permittivity is small compared to the real part, only the real part of permittivity changes with soil water content, and if the real part is close to the apparent dielectric permittivity K_a (*effective bulk permittivity*), then water content can be evaluated by means of empirical formulas based on known value of K_a (Evett et al., 2005; Topp et al., 1980). Evaluation of the dielectric permittivity of a medium from its reflection response is an inverse problem in which the medium propagation behavior is used to infer its constitutive relations (Feng et al., 1999; Heimovaara, 1994; Lin, 2003; Oswald et al., 2006).

Owing to this application, over the past twenty years great efforts have been spent on the calibration of the TDR system, i.e. the relationship between apparent dielectric permittivity and soil water content (Hansson & Lundin, 2006; Roth et al., 1990; Topp et al., 1980), on the design and testing of various type of probes (Canone et al., 2009; Evett et al., 2006; Robinson et al., 2005); and on the methods to solve the inverse problem of estimating permittivity from reflection responses (Heimovaara, 1994; Oswald et al., 2006).

Regardless of the inversion method used, the model of the measurement system (relating measured waveforms to the unknown permittivity to be estimated) is the instrument enabling the permittivity estimation from the reflection response. The modeling of the TDR measurement system received, therefore, a great deal of attention in the past (Heimovaara, 1994; Lin, 2003). In spite of the advances in modeling of the TDR setup and in evaluation of permittivity from the TDR response, the intrinsic limitations introduced by the TDR

measurement setup on estimation of permittivity spectrum have rarely been addressed. If the information about electrical properties of the sample under test is lost due to the characteristics of the measurement system, it is not possible to retrieve such an information whatever the accuracy of the inversion method used.

In this study the limitations introduced by the TDR measurement setup and the effect of wave attenuation along the TDR probe are addressed. To this end, a measurement setup easy to model has been chosen. In this setup, a coaxial airline instead of the probes generally used for TDR measurements (two or three arms sensor as in Fig. 1, right) is considered. A coaxial airline can be modeled as a TEM transmission line (Pozar, 2005), whereas other types of probes generally used in TDR measurements can be only modeled by numerical techniques. Moreover, the actual signal launched by the TDR instrument and not only an ideal unit voltage step has been considered in the model as an input signal. Thanks to this accurate model and using a parametric inversion approach, it was possible to obtain a very good fitting of several reference liquids and various sand and clay samples with different water content and to determine their permittivity and conductivity. Then, with the aid of a frequency domain analysis on the same model but with some simplifications, the limitations introduced by the TDR measurement setup are studied in details. It will be shown that the probe length sets an upper limit to the frequency that can be used and that this limit is independent from the well-known impact of the TDR instrument bandwidth (Savi et al., 2010).

In more details, an equivalent circuit of the TDR measurement setup based on transmission line theory is introduced. Signals traveling along the connecting cables and probe (an open-ended ideal coaxial line) are described as Transverse Electro-Magnetic (TEM) waves and the various discontinuities (output port of the instrument, cable-probe connection) are kept into account by means of a scattering matrix description (Pozar, 2005). A parametric representation of the permittivity spectrum as a one-pole real rational model (Debye's permittivity model, (Hasted, 1973)) is assumed and its parameters are estimated by fitting the model response to the measured response. This approach has been adopted because it is less sensitive to measurements errors in the high-frequency range with respect to *direct inversion* techniques. This accurate model (in which the finite rise-time and the aberration of the real input signal, and the junction between probe and port of the TDR instrument are kept into account) and the *parametric inversion* approach lead to an accurate evaluation of permittivity. Then, a simplified model of the TDR measurement system, where an ideal voltage step is applied to an ideal cable connected to the probe is considered. In this case, the real signal of the generator and the various discontinuities are not kept into account. The reflection coefficient at the probe input port is written as a function of the model parameters in frequency domain and decomposed into a sequence of echoes. Analysis of the second echo points out the role of the probe attenuation and a threshold on the attenuation of the working condition of the measurement setup. Two types of TDR waveforms (low-attenuation and high-attenuation) can be identified. Transition between the two types of waveforms is controlled by the wave attenuation along the probe. Starting from the ideal model of measurements setup, simple relations to evaluate the low-frequency permittivity (ϵ_s) and the high-frequency permittivity (ϵ_∞) directly from characteristic points of the waveform are introduced.

In this chapter, the following topics are presented in details: an accurate model of the TDR measurement setup based on a coaxial airline probe together with a fitting procedure to obtain the complex permittivity (see Section 2 and 3); a simplified model enabling the analysis of properties and limitations of the measurement setup (see Section 4); simple formulas to

evaluate permittivity and conductivity from the TDR response (see Section 5). This analysis is applied to some reference liquids (deionized water and methanol) and various sand and clay soil with different water content (see Section 6).

2. TDR measurement system

A time-domain reflectometer (see Fig. 1) consists mainly of a very fast rise time pulse generator and an oscilloscope. The step generator produces a positive-going incident wave that is fed into the transmission system under test (probe). The step travels down the transmission line at the velocity of propagation of the line. If the load impedance is equal to the characteristic impedance of the line, no wave is reflected. If a mismatch exists at the load, part of the incident wave is reflected.

The TDR system (TDR instrument and probe) can be modeled by an ideal transmission line (Pozar, 2005) and the reflected voltage detected from the instrument can be obtained with the help of the bouncing diagram of Fig. 2. In the reflected voltage, the first falling edge represents the partial reflection coefficient at the discontinuity between the output port of the instrument and the transmission line, the stair-case is due to the multiple reflections along the line. Step amplitudes depend on permittivity, time delay between a step and the next one depends on permittivity and on the physical length of the line. Therefore, in this ideal case in which the permittivity is constant with the frequency, it is possible to find the value of the permittivity from the TDR waveform. When permittivity is a function of frequency, the TDR response is similar to an ideal case, but the problem should be faced with a frequency domain approach.

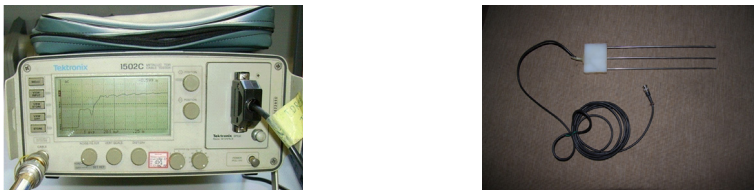


Fig. 1. Left: The frontal panel of the Tektronix 1502B reflectometer with rise time $t_r = 0.3$ ns. Right: A three arms probe.

The basic scheme for the analysis of the propagation along the probe in the frequency domain is shown in Fig. 3. The system's response can be calculated by means of the convolution of the input signal $v_0(t)$ and the system impulsive response $h(t)$ as:

$$r(t) = \int_{-\infty}^{\infty} v_0(t - \tau) h(\tau) d\tau \quad (1)$$

In the frequency domain the convolution can be written as:

$$R(f) = V_0(f) H(f) \quad (2)$$

where $R(f)$, $V_0(f)$ and $H(f)$ are the Fourier transforms of $r(t)$, $v_0(t)$ and $h(t)$, respectively. $H(f)$, and thus $h(t)$, are functions of the dielectric behavior of the soil sample and the properties of the probe, such as length and characteristic impedance. As $v_0(t)$ and $r(t)$ (and

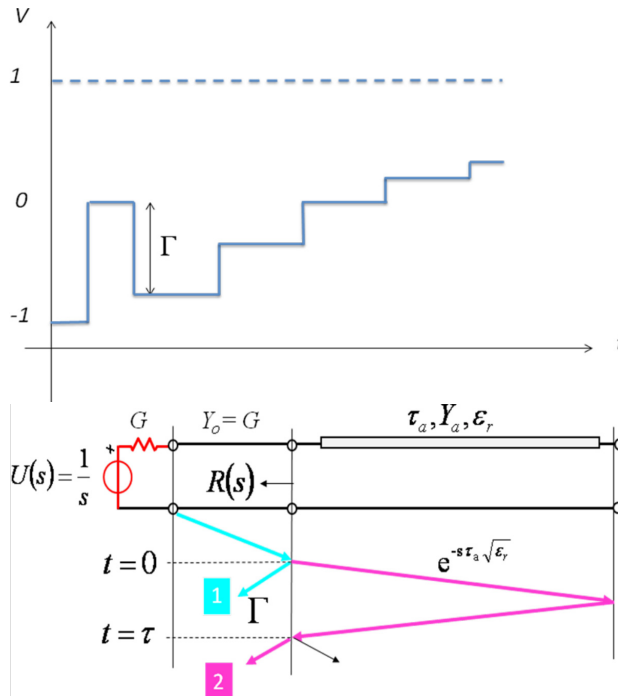


Fig. 2. TDR response and bouncing diagram of the TDR system.

therefore their Fourier transforms $R(f)$, $V_0(f)$ are known, we can calculate $H(f)$ by means of eq. (2).

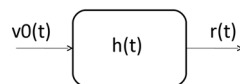


Fig. 3. Linear system analysis.

3. Accurate model of the TDR measurement setup

The TDR measurement set up has been modeled by the chain network of Fig. 4. The system has been divided into 6 parts and characterized separately. In this model, the TDR source composed by the signal generator (1) and the oscilloscope (2) is represented by a matched source with internal admittance G , driving the network with the same waveform measured in the actual TDR instrument. The finite rise time and the aberration of the real probing signal are thus kept into account. The coaxial cable (3) that connects the instrument to the probe is modeled by an ideal lossless transmission line. Part 4 is the output port of the instrument and is represented by a lumped-distributed 2-port element. This two-port element has been identified by fitting the response of the chain network to the response measured with the probe left empty (5). Part 5 and 6 are the probe itself filled with the soil sample under test and

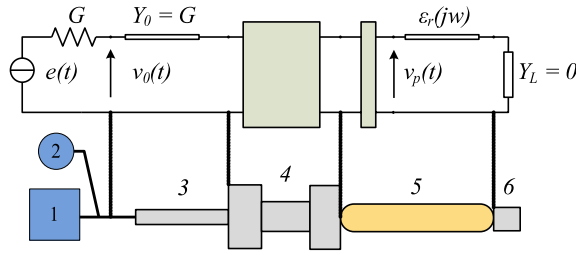


Fig. 4. Block diagram of a TDR measurement system and its chain network model.

the probe termination. Parts (1)-(3) are included in the TDR instrument, whereas parts (4)-(6) form the device whose reflection response is measured.

The unknown permittivity is described by the one-pole Debye's permittivity model modified in order to keep into account the conductivity γ of the dielectric under test:

$$\epsilon_r(j\omega) = \epsilon_\infty + (\epsilon_s - \epsilon_\infty) / (1 + \frac{j\omega}{\omega_{rel}}) + \frac{\sigma_s}{j\omega} \quad (3)$$

where ϵ_∞ , ϵ_s and $\omega_{rel} = 2\pi f_{rel}$ are the Debye's parameters. The four parameters ($\epsilon_s, \epsilon_\infty, \omega_{rel}, \sigma_s$) of eq. (3) are estimated by a parametric inversion approach, i.e. by fitting the model response to the measured one. Other models can be used, such as multi-pole equations and the Cole-Cole equations. Those methods have improved the fitting accuracy, but the accuracy gained does not worth the increase of complexity (Heimovaara, 1994; Huisman et al., 2004). As an example, the estimation of the permittivity via waveform fitting based on the transmission line model previously described is applied to two reference liquids: deionized water and methanol. Results are shown in Fig. 5 and Fig. 6, respectively. The solid line curves are the measurements obtained by an HP 54120B digitalizing oscilloscope (see subsection 6.1). The dashed line curves are obtained by fitting the response of the transmission line model described in this Section to the measured curves. The best fit of the measured responses ($T = 25^\circ$) is obtained with $\epsilon_s = 78$, $\sigma_s = 0.3$ mS/m for deionized water (Lide, 1992), and $\epsilon_s = 32$, $\sigma_s = 0.1$ mS/m for methanol (Weerts et al., 2001).

4. Simplified model and probe attenuation

In order to point out the inherent properties of the TDR responses, we consider the simplified model shown in Fig. 7, where an ideal voltage step (infinite bandwidth) $u(t)$ ($U(s) = 1/s$ in the frequency domain) is applied to an ideal cable of characteristic admittance Y_0 connected to the probe. The probe is an open-ended ideal coaxial line and can be modeled as a TEM transmission line of characteristic admittance and time delay of the empty airline Y_a and τ_a , respectively. In this lossless, simplified model, the measured quantity is the time evolution of the backward wave at the probe input, i.e., $r(t) = L^{-1}[R(s)] = L^{-1}[S_{11}(s)(1/s)]$ where S_{11} is the reflection coefficient at the cable-probe discontinuity, L^{-1} is the inverse Laplace transform operator, and lower-case and upper-case letters are used to indicate transform pairs. The features of both the measured waveform $r(t)$ and its spectrum $R(s)$ are investigated and their relationship to the permittivity parameters ($\epsilon_s, \epsilon_\infty, \omega_{rel}, \sigma_s$) and to the probe parameters (Y_a ,

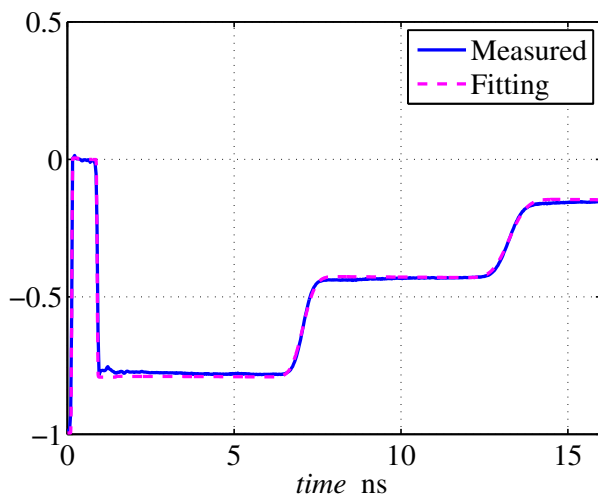


Fig. 5. TDR measurements (solid line) and fitting (dashed line) for a sample of deionized water. The measured data are obtained with an HP 54120B digitalizing oscilloscope.

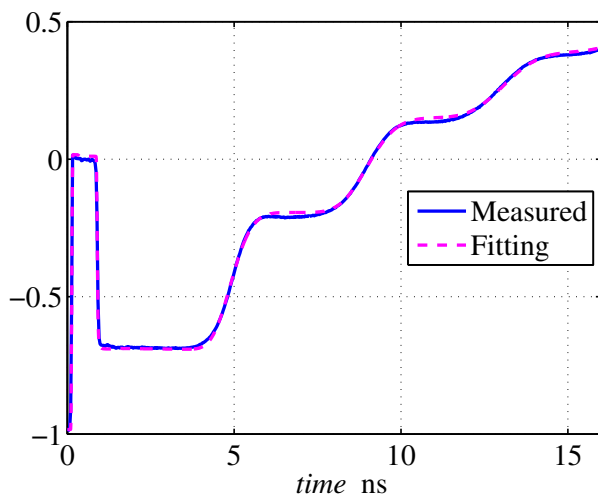


Fig. 6. TDR measurements (solid line) and fitting (dashed line) for a sample of methanol. The measured data are obtained with an HP 54120B digitalizing oscilloscope.

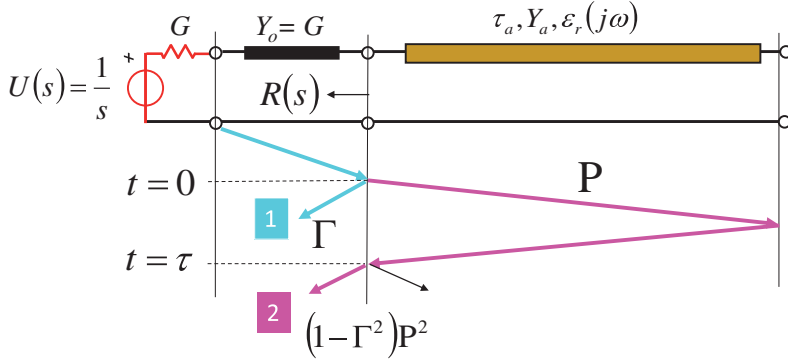


Fig. 7. Simplified transmission line model of the TDR measurement system and bouncing diagram. First contribution ($\bar{\Gamma}$: the signal reflected at the input port of the probe (partial reflection coefficient); second contribution $(1 - \bar{\Gamma}^2(S)) \bar{P}^2(S)$: the signal transmitted and traveling forward and backward along the probe.

τ_a) are pointed out. To this end, the following normalized quantities are used:

$$\begin{aligned} T &= t \omega_{rel}, & S &= s / \omega_{rel}, & \mathcal{Y} &= Y_a \sqrt{\epsilon_\infty} / Y_o \\ \mathcal{T} &= \tau_a \sqrt{\epsilon_\infty} \omega_{rel}, & \eta &= \epsilon_s / \epsilon_\infty \end{aligned} \quad (4)$$

where T and S are the normalized time and complex frequency, respectively. The analysis is based on the decomposition of the normalized reflection coefficient \bar{S}_{11} into a sequence of echoes (see the bouncing diagram in Fig. 7):

$$\begin{aligned} \bar{S}_{11}(S) &= \bar{\Gamma}(S) + (1 - \bar{\Gamma}^2(S)) \bar{P}^2(S) \\ &\quad (1 - \bar{\Gamma}^2(S)) (-\bar{\Gamma}) \bar{P}^4 + \dots \end{aligned} \quad (5)$$

where

$$\bar{\Gamma}(S) = \frac{1 - \mathcal{Y} \sqrt{\bar{\epsilon}}}{1 + \mathcal{Y} \sqrt{\bar{\epsilon}}} \quad (6)$$

is the probe partial reflection coefficient (the portion of the input signal that is reflected back from the first discontinuity, see Fig. 7, contribution 1) and

$$\bar{P}(S) = \exp\{-2\mathcal{T}S\sqrt{\bar{\epsilon}(S)}\} \quad (7)$$

is the propagation factor as functions of the normalized frequency and $\bar{\epsilon} = 1 + (\eta - 1)/(1 + S)$ and $S = j\Omega$, where Ω is the normalized angular frequency. The first term of equation (5), $\bar{H}_1(S) = \bar{\Gamma}(S)$, is the network function relating the incident wave to the wave reflected by the cable-probe discontinuity. The second term, $\bar{H}_2(S) = (1 - \bar{\Gamma}^2(S)) \bar{P}^2(S)$, relates the incident wave to the wave reflected by the probe load and so on. In the time domain, these terms start at $T = 0, 2\mathcal{T}, 4\mathcal{T}, \dots$, and give rise to the echoes forming the observed response, i.e., $\bar{r}(T) = \bar{r}_1(T) + \bar{r}_2(T) + \dots$

4.1 Low-attenuation condition

In order to study the properties of the simplified model responses, it is convenient to focus on the second echo $\bar{r}_2(T)$, because it is the simplest term containing information on both the probe-cable discontinuity and on the propagation in the dielectric. The behavior of the second echo is decided by the network functions $\bar{H}_2(S)$ and, in particular, by the square propagation factor $\bar{P}^2(S) = \exp(-2TS\sqrt{\bar{\epsilon}})$ where $\bar{\epsilon} = 1 + (\eta - 1)/(1 + S)$. Figure 8a,b shows $|\bar{P}^2(j\Omega)|$ for $T = 6, 15, 40$ and $\eta = 1.5, 3$. (Panel b is a close-up view of the middle lower part of panel a). For growing T and η values, the high-frequency magnitude of $|\bar{P}^2|$ becomes negligibly

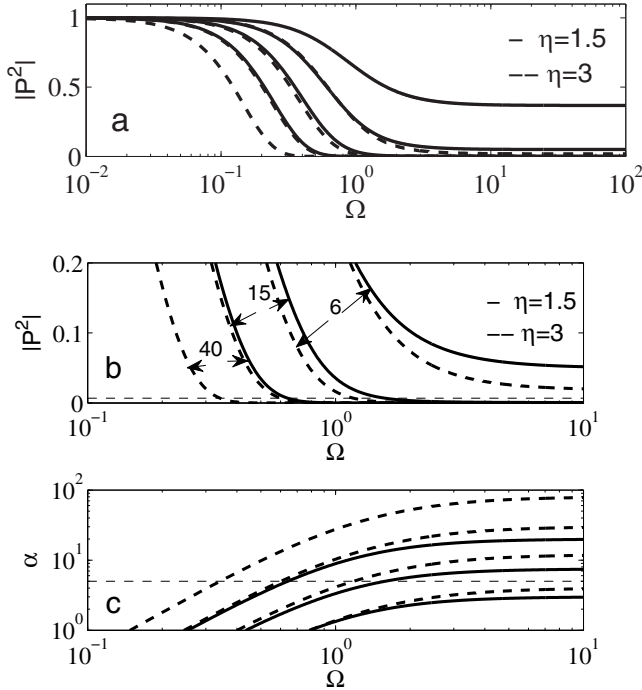


Fig. 8. Magnitude of the propagation factor (a and b) and attenuation constant (c) versus normalized angular frequency for $T = 6, 15, 40$ and $\eta = 1.5, 3$. Panel b is a close-up view of panel a. The dashed horizontal lines of panel b and c indicate the threshold level $|\bar{P}^2| = \exp(-5)$ and $\zeta = 5$, respectively.

small and, therefore, \bar{H}_2 becomes a bandlimited function. This bandlimiting effect is due to the imaginary part of $\bar{\epsilon}(j\Omega)$, that is responsible for the attenuation constant of \bar{P}^2 :

$$\alpha = -\Re\{j2\Omega T \sqrt{\bar{\epsilon}(j\Omega)}\} = -2\Omega T \Im\left\{\sqrt{1 + \frac{\eta - 1}{1 + j\Omega}}\right\} \quad (8)$$

The attenuation constant is plotted vs. frequency in Fig. 8c. Every attenuation curve is composed of a quadratic low-frequency part (the constant slope part in the bi-logarithmic scales of Fig. 8c) and by a constant high-frequency part. The constant part arises from the high

frequency behavior of $\Im m\{\sqrt{\tilde{\epsilon}}(j\Omega)\}$, that is inversely proportional to Ω . The high-frequency asymptotic value of α is:

$$\xi = \lim_{\Omega \rightarrow \infty} \alpha(j\Omega) = \mathcal{T}(\eta - 1) \quad (9)$$

and the asymptotic value of $|\bar{P}^2|$ is $\exp(-\xi)$. For example, if $\xi = 5$, the asymptotic value of $|\bar{P}^2|$ is close to 6.7×10^{-3} and can be considered small. The relation between the $|\bar{P}^2|$ and α curves of Fig. 8 is explained by this property. Bandlimited propagation factors are associated to attenuation curves with $\xi > 5$, and the propagation factors become small where their attenuation curves overpass this threshold level (see Fig. 8a,b,c). In the following, we use the term *high-attenuation* to indicate the case $\xi > 5$. Measurement setups working in high-attenuation conditions have \bar{H}_2 functions with small high frequency magnitudes. In this case, the network functions of the higher order echoes have small high-frequency magnitudes as well, because they include powers of the factor \bar{P}^2 . As a consequence, in high-attenuation conditions, the high-frequency content of the measured TDR waveforms is low and the relation with the high-frequency permittivity spectrum is expected to be weak. According to this analysis, measurement setup operating in the low-attenuation domain ($\xi < 5$) are preferable.

As an example, consider the TDR waveforms corresponding to the low and high-attenuation cases shown in Fig. 9. The parameters are $\epsilon_s = 12$, $\epsilon_\infty = 6$, $f_{rel} = 0.7$ GHz, $Z_a = \sqrt{\mathcal{L}/\mathcal{C}} = 77 \Omega$. In the low-attenuation condition $\tau_a = 0.34$ ns and $\xi = 3.7$, whereas for high-attenuation $\tau_a = 1$ ns and $\xi = 11$. When the wave reflected from the probe end has harmonic components with significant amplitude for frequency larger than f_{rel} the observed TDR waveforms are of low-attenuation type. This reflection behavior is illustrated in Fig. 9a, where the solid line curve is the magnitude of the network function of the first echo from the probe end for a low-attenuation case and the dotted straight line corresponds to the relaxation frequency (the bandwidth of the instrument source is larger than the relaxation frequency of the dielectric under test). Similarly, when the harmonic components of the wave reflected from the probe end have negligible amplitude for frequency larger than f_{rel} , the TDR waveform are of high-attenuation type (dashed curve of Fig. 9a). The bandwidth of the waveforms of high-attenuation type is therefore inherently limited to f_{rel} , regardless of the source bandwidth, and these waveforms are scarcely sensitive to the high-frequency parameters of the permittivity. The two types of TDR response can be easily identified because, in the low-attenuation case, the rising edge corresponding to the first echo from the probe end is asymmetric and steep, whereas, in the high-attenuation case, the edge is symmetric and gradual (see Fig. 9b, where $\rho(t) = 2v_o(t)/e_f - 1$, e_f asymptotic value of $e(t)$). Remembering that $\mathcal{T} = \tau_a \sqrt{\epsilon_\infty} \omega_{rel}$ and $\eta = \epsilon_s/\epsilon_\infty$, the low-attenuation condition can be expressed in physical parameters as:

$$\xi = \tau_a \omega_{rel} \frac{\epsilon_s - \epsilon_\infty}{\sqrt{\epsilon_\infty}} < 5 \quad (10)$$

or, equivalently, as:

$$2\tau_a \sqrt{\epsilon_\infty} < 10 \epsilon_\infty / \omega_{rel} (\epsilon_s - \epsilon_\infty) \quad (11)$$

where $2\tau_a \sqrt{\epsilon_\infty}$ is the probe round trip delay. This means that $2\tau_a \sqrt{\epsilon_\infty}$, i.e., the probe electrical length, must be limited in order to obtain low-attenuation operation. As a consequence of (11), two limitations on the instrument resolution and on the length of the probe should be taken

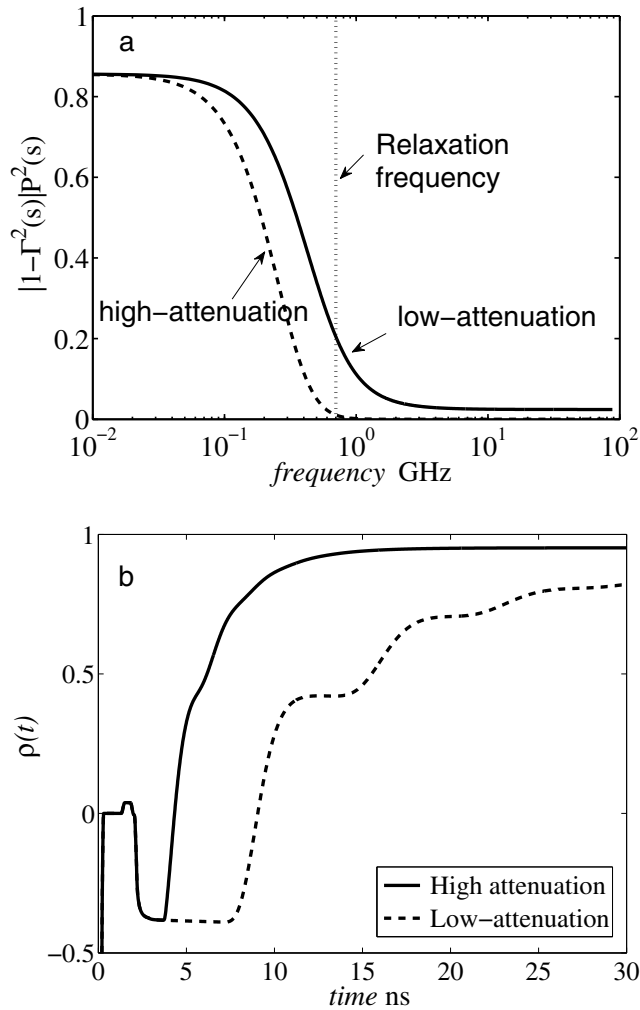


Fig. 9. Panel a : magnitude of the network function of the first echo from the probe end for a low-attenuation case (solid line) and an high-attenuation case (dashed line). Panel b: TDR waveforms corresponding to the response of panel a. Parameter values: $\epsilon_s = 12$, $\epsilon_\infty = 6$, $f_{rel} = 0.7$ GHz, $Z_a = \sqrt{\mathcal{L}/\mathcal{C}} = 77 \Omega$, $\tau_a = 0.34$ ns (low-attenuation) and $\tau_a = 1$ ns (high-attenuation). The responses of this figure hold for an ideal step input.

Medium	f_{rel}	ϵ_s	ϵ_∞	$10\epsilon_\infty/\omega_{rel}(\epsilon_s - \epsilon_\infty)$	ref.
deionized water	17 GHz	80	4.22	5.2ps	(Heimovaara, 1994)
wet sand	7 GHz	15	3	57ps	(Feng et al., 1999)
ethanol	0.782 GHz	25.2	4.52	445ps	(Heimovaara, 1994)
dry sand	7 GHz	3	2.8	5.25ns	(Feng et al., 1999)

Table 1. Debye's parameter values for some typical dielectrics. $2\tau_a\sqrt{\epsilon_\infty}$ is the maximum round trip delay.

into account. The instrument resolution must be significantly finer than $10\epsilon_\infty/\omega_{rel}(\epsilon_s - \epsilon_\infty)$. In practice, the resolution of TDR instruments is limited by the rise time of their sources that is on the order of $150 \div 200$ ps for conventional field instruments and of 30 ps for high-end instruments, and low attenuation measurements can be obtained only for dielectric with $\omega_{rel}(\epsilon_s - \epsilon_\infty)/\epsilon_\infty$ small enough. On the other hand, a too short probe ($l = \tau_ac$) cannot be considered both for practical reasons and because the transmission line model requires the cross-section to be much smaller than the length of the probe. Some examples of parameter values are listed in Tab. 1. The ethanol can be considered as a limit case. In fact, the maximum round trip delay is 445 ps and can be detected by a standard TDR instrument, and the length of the probe in this case should be 3 cm.

4.2 Parametric analysis

In this section, we analyse the variation of the parameters (ϵ_s , ϵ_∞ , ω_{rel} , σ_s) of the Debye permittivity equation (3) on the TDR waveform. Results are shown in Figs.10-13. These examples are of high-attenuation type. It is worthwhile to notice that none of the parameters of the Debye permittivity affect the first falling edge of the responses. Hence, the parameter estimation is not affected by model errors influencing this part of the response (*e.g.*, the element representing the probe input section). The static permittivity, ϵ_s , dominates the propagation effects, *i.e.*, it roughly defines the probe characteristic impedance and propagation speed. In fact, Fig. 10 shows that ϵ_s modifies the position of the first rising edge (probe delay) and its amplitude (probe characteristic impedance). The parameter f_{rel} controls the slope of the rising edges, thereby it complicates the assessment of the probe delay and ϵ_s estimation based on probe delays (Heimovaara, 1994). Besides, when the effect of ϵ_∞ is not negligible (Fig. 11), it mixes up with the effect of f_{rel} , as they affect the same part of the responses. Finally, the electrical conductivity σ_s affects the long-time behaviors of the responses, by reducing levels and amplitudes of the reflections from the probe end (Fig. 13). This is consistent with the low-frequency lossy effect of the conductivity parameter. Unfortunately, growing values of σ_s reduce the sensitivity of responses to all parameters, thereby increasing the uncertainty on parameters estimations.

5. Simple formulas to evaluate the permittivity from the TDR response

The two major features of TDR waveforms are the travel time in the probe and the response 'late' time amplitude that are directly related to the apparent dielectric constant and to the soil electrical conductivity. Several studies in the literature have aimed at determining a good method to evaluate the travel time from the TDR curve. Starting from the ideal model of the measurements setup and the frequency domain analysis previously introduced, simple

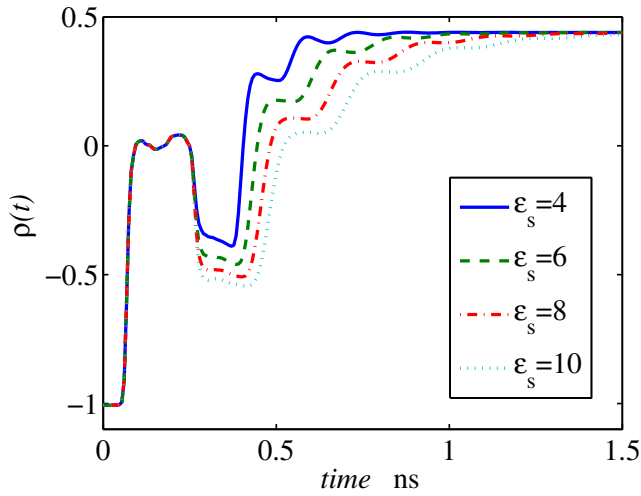


Fig. 10. Model response for different values of ϵ_s (4, 6, 8, 10). Other parameter values are $\omega_{rel} = 20 \cdot 10^9$; $\epsilon_\infty = 3$; $\sigma_s = 1 \cdot 10^{-2}$ S/m.

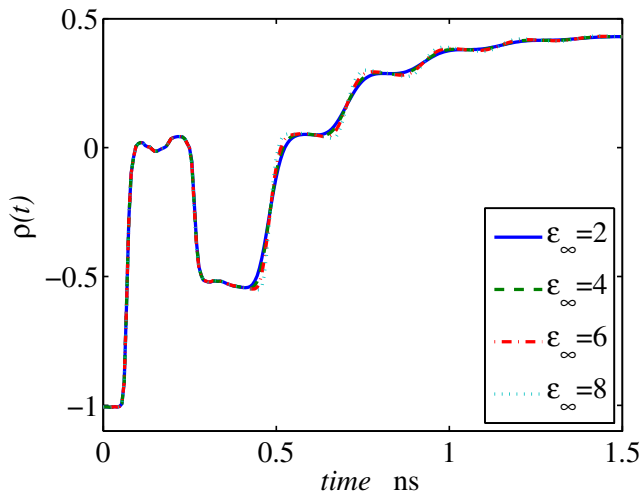


Fig. 11. Model response for different values of ϵ_∞ (2, 4, 6, 8). Other parameter values are $\omega_{rel} = 20 \cdot 10^9$; $\epsilon_s = 10$; $\sigma_s = 1 \cdot 10^{-2}$ S/m.

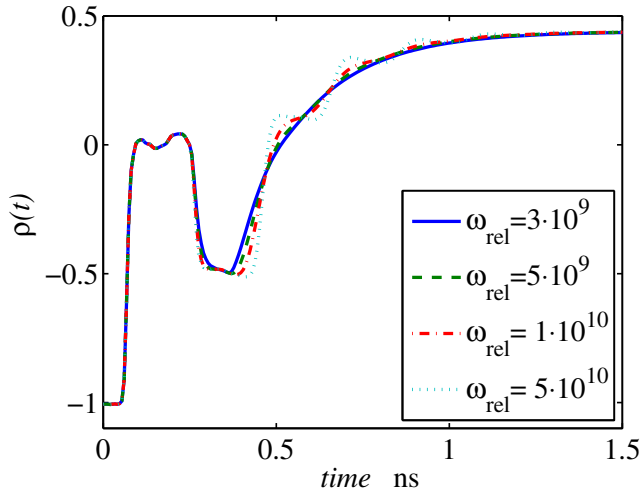


Fig. 12. Model response for different values of ω_{rel} ($3 \cdot 10^9, 5 \cdot 10^9, 1 \cdot 10^{10}, 5 \cdot 10^{10}$). Other parameter values are $\epsilon_\infty = 8$; $\epsilon_s = 2.5$; $\sigma_s = 10^{-2} \text{ S/m}$.

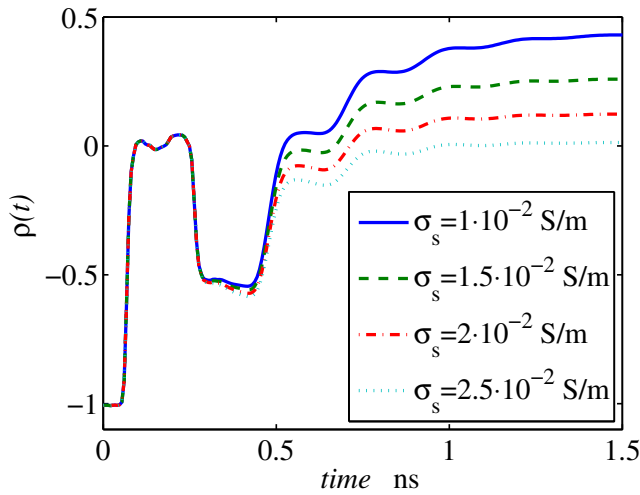


Fig. 13. Model response for different values of σ_s ($1 \cdot 10^{-2}, 1.5 \cdot 10^{-2}, 2 \cdot 10^{-2}, 2.5 \cdot 10^{-2}$) S/m. Other parameter values are $\omega_{rel} = 20 \cdot 10^9$; $\epsilon_s = 10$; $\epsilon_\infty = 3$.

relations to evaluate the low-frequency permittivity (ϵ_s) and the high-frequency permittivity (ϵ_∞) directly from the characteristic points of the waveform are introduced.

From equation (6), remembering that $\mathcal{Y} = Y_a \sqrt{\epsilon_\infty} / Y_o$ and that

$$\bar{\epsilon}(S) = 1 + (\eta - 1) / (1 + S) \sim \eta = \frac{\epsilon_s}{\epsilon_\infty} \quad (12)$$

the low-frequency permittivity ϵ_s can be estimated as:

$$\epsilon_s \sim \left[\frac{Y_0 (1 - h)}{Y_a (1 + h)} \right]^2 \quad (13)$$

This formula can be used to determine the low-frequency permittivity instead of the standard method based on the delay of the inflection point of the first rising edge (t_b) that gives:

$$\epsilon_s \sim \left(\frac{t_b}{2\tau_a} \right)^2 \quad (14)$$

When a low-attenuation condition holds (small ζ values) the rising edges are asymmetric and start at $2\tau_a \sqrt{\epsilon_\infty}$. In this case, also the value of ϵ_∞ can be determined as:

$$\epsilon_\infty \sim \left(\frac{t_a}{2\tau_a} \right)^2 \quad (15)$$

where t_a is the corner of the first rising edge (see Fig. 14).

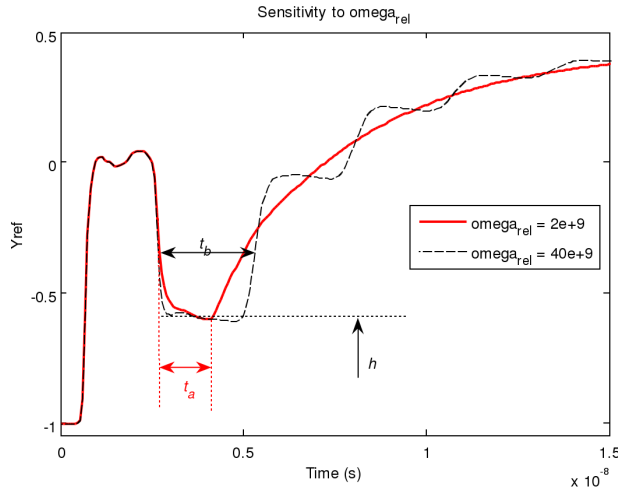


Fig. 14. Definition of the parameters h , t_a , t_b .

6. Soil measurements examples

6.1 Measurement setup description

Two different instruments were used in order to measure the time-domain response: a Tektronix 1502B reflectometer with rise time $t_r = 0.3$ ns (horizontal setting 0.1 m per division and a propagation velocity setting of 0.99), 13-bit data acquisition (range from 0 to 8192) (see Fig. 1); and a digitalizing oscilloscope HP54120B with rise time $t_r = 10$ ps (see Fig. 15 left). The samples were inserted in a coaxial probe terminated on a $50\ \Omega$ load (Maury Microwave Airline, model no. 2653S10, length $\ell = 10.5$ cm, shield and inner conductor radii 3.5 mm and 1.5 mm, respectively, dc-resistance of inner conductor $9.4\ \text{m}\Omega/\text{m}$, see Fig. 15 right). In the case of Tektronix 1502B, the acquisition of the waveforms by the computer was done by means of a serial cable and the software WinTDR 6.1 developed by the Soil Physics Group at Utah State University, Logan Utah, USA (<http://www.usu.edu/soilphysics/wintdr/>). In the case of the digitalizing oscilloscope HP54120B with a GPIB communications (IEEE 488.2 standard), a data acquisition interface was developed with the help of Labview (<http://www.ni.com/labview/>).



Fig. 15. The frontal panel of the HP 54120B digitalizing oscilloscope with rise time $t_r = 10$ ps (left). The coaxial probe (Maury Microwave Airline, model no. 2653S10, length $\ell = 10.5$ cm used in the measurement setup (right).

6.2 Example of parametric inversion in sand samples

In this section, the parametric inversion procedure is applied to the TDR response of an almost dry sand sample (3.4% volumetric water content) and to the response of a sand sample with 25% volumetric water content. In both cases, the TDR responses have been obtained with a Tektronix 1502B reflectometer. These waveforms are of low-attenuation waveform and, according to the analysis of the previous Section, their estimation problem is expected to be well conditioned also for the high-frequency part of the permittivity.

The measured results obtained in the first case (dry sand) are shown in Fig. 16 (solid line). The model response that best fits the measured curve is also shown (dashed line) and the estimated values of the permittivity parameters are: $\epsilon_s = 3.18$, $\epsilon_\infty = 2.69$, $f_{rel} = 413$ MHz and $\sigma_s = 6.36 \cdot 10^{-4}$ S/m. These parameter values correspond to $\xi = 0.28$, confirming that the measured response is of low-attenuation type, as expected.

The TDR response of the sand sample with 25% water content is shown in Fig. 17 (solid line). The TDR response of this example as well looks like a low-attenuation waveform and its estimation problem is expected to be well conditioned for the high-frequency part of the permittivity. The model response that best fits the measurement is shown in Fig. 17

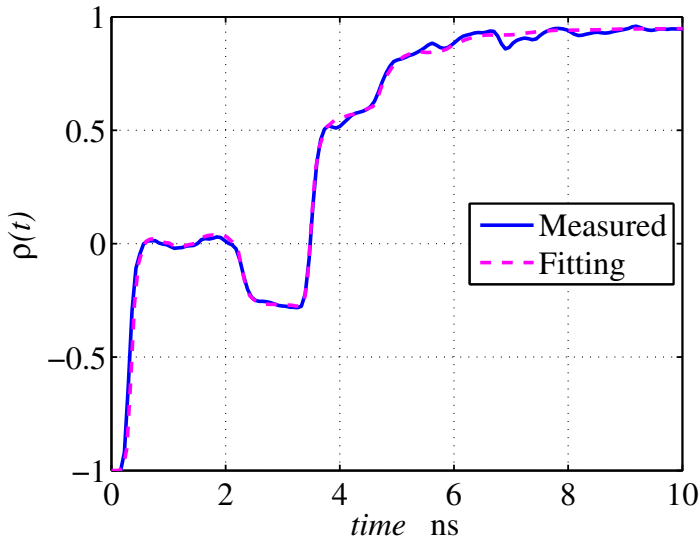


Fig. 16. Measured TDR response for a sand sample (solid line) and the best fit response of the accurate model (dashed line). Permittivity parameters: $\epsilon_s = 3.18$, $\epsilon_\infty = 2.69$, $f_{rel} = 413$ MHz and $\sigma_s = 6.36 \cdot 10^{-4}$ S/m.

(dashed curve) and the estimated values of the permittivity parameters are $\epsilon_s = 12$, $\epsilon_\infty = 8.4$, $f_{rel} = 1.38$ GHz and $\sigma_s = 0.007$ S/m. These parameter values correspond to $\zeta = 3.7$, confirming that the measured response is of low-attenuation type as expected.

The condition of the estimation problem is decided by the behavior of the error function around the estimated parameter values. An indicator of this behavior can be obtained by plots of the function over planes of the parameter space. The error function of the 25% water content sample over the plane $(\epsilon_\infty, f_{rel})$ is shown in Fig. 18 and looks as a well behaved convex surface, thereby suggesting the good condition of the estimation of the high-frequency parameters.

6.3 Three methods for the estimation of permittivity in sand and clay samples

In this section, three different methods for the determination of the low-frequency permittivity ϵ_s are compared. In the first method, the permittivity is calculated from the travel time of the TDR signal along the probe (as in the method described in (Topp et al., 1980)), but the starting point and ending point of the travel time is determined from the apex of the derivative of the waveform of the reflected signal (derivative method) (Robinson et al., 2005). In the second case, the permittivity is evaluated by using eq. (14-15) (low-level method), whereas in the third case the permittivity is estimated via a parametric inversion approach based on the model of the measurement setup described in Section 3 (fitting).

To this end, the TDR response of two set of sand and clay samples with different water content have been measured. After a process of weighting and drying, the water content of each sample was determined as:

$$\theta_{water} = \frac{P_w - P_d}{V_{probe}} \quad (16)$$

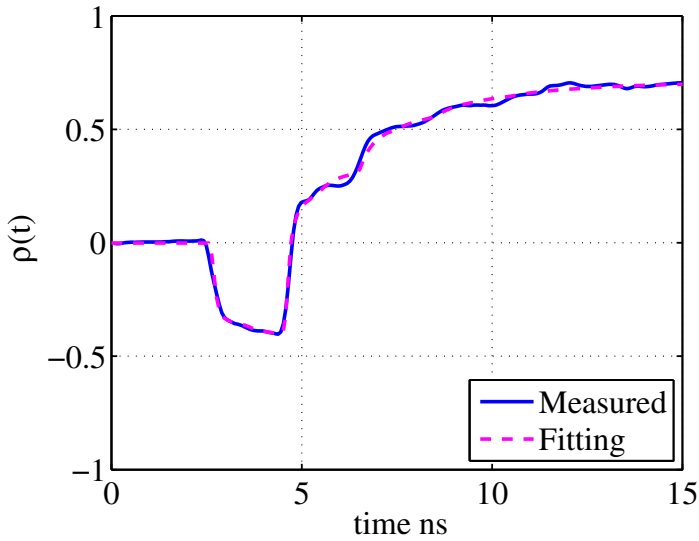


Fig. 17. Measured TDR response for a sand sample with 25% water content (solid line) and the best fit response of the accurate model (dashed line). Permittivity parameters: $\epsilon_s = 12$, $\epsilon_\infty = 8.4$, $f_{rel} = 1.38$ GHz and $\sigma_s = 0.007$ S/m.

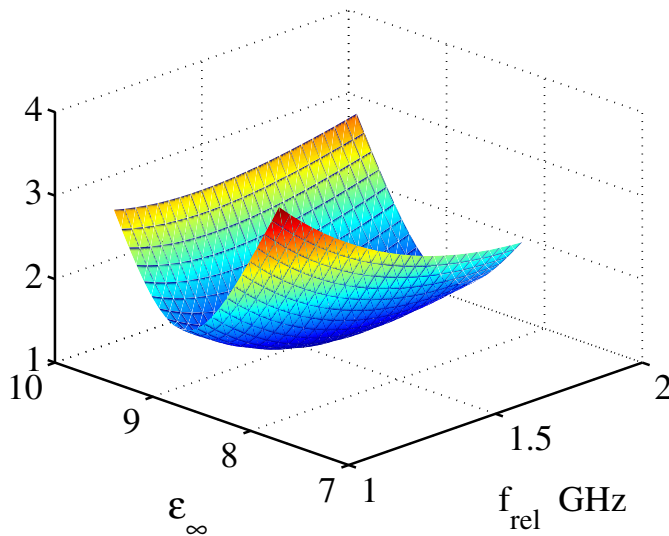


Fig. 18. Error surface in the $(\epsilon_\infty, f_{rel})$ plane for a sand sample with 25% water content.

where P_w is the wet weight, P_d is the dry weight, and V_{probe} is the volume of the probe. The results obtained with these methods are shown in Fig. 19. Sand samples correspond to a high value of ξ (high-attenuation case), whereas in case of clay samples the value of ξ is small (low-attenuation case). As it was expected, the value of ϵ_s increases with water content. The low-level method based on eq. (14-15) works as well as the more complicate derivative method and fitting method. Note that sensitivity of the low-level method increases as permittivity increases, and that sensitivity in the high-attenuation case increases with the frequency. These considerations explain the inaccuracies of the low-level method for a high water content in case of sand samples of Fig. 19, Panel a.

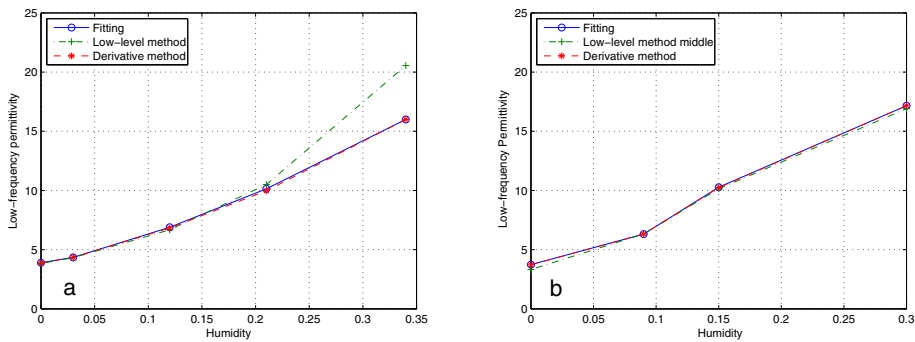


Fig. 19. Low-frequency permittivity values obtained with the fitting, low-level and derivative method for sand samples (Panel a) and clay samples (Panel b) as a function of water content.

7. Conclusion

In this analysis, an accurate model of the TDR measurement setup has been introduced. A parametric representation of unknown permittivity is introduced and its parameters are estimated by fitting the model response to the TDR measured response. This accurate model and the parametric inversion approach lead to an accurate evaluation of soil permittivity. The values of Debye's model parameters have been related to the features of the TDR waveform. The role of probe attenuation in estimation of dielectric permittivity spectrum from TDR waveforms has been studied. The analysis is based on an simplified model of the measurement setup and on Debye's model of the unknown permittivity. Main result is that two types of TDR waveforms (low-attenuation and high-attenuation) can be identified. The shape of the edges in TDR waveform indicates whether the measurement setup works in low- or high-attenuation condition. Transition between the two types of waveforms is controlled by the wave attenuation along the probe. Low-attenuation operation can be obtained by using short probes and it yields waveforms that are more sensitive to the high-frequency behavior of the permittivity, since their harmonic content extends beyond the relaxation frequency f_{rel} . For small- ξ values, both ϵ_s and ϵ_∞ can be estimated from the TDR waveform, whereas for large- ξ values, only ϵ_s can be estimated.

Simple relations to evaluate the low-frequency permittivity directly from the TDR waveforms are introduced. These formulas are easy to use, and in good agreement with the results obtained with a derivative method based on the travel time of TDR signal along the probe

and with the results obtained using a parametric inversion approach based on an accurate model.

There are still many open problems and future works in the TDR technique applied to estimation of soil permittivity:

- Modeling of the system and in particular of the input port - probe transition, could be improved with the help of Layer Peeling techniques (Rautio, 1991; Tripathi & Jong, 1992).
- Fitting the modeled response to the measured response can be refined with numerical techniques.
- Implementation of a multi-pole Debye's equation, or another model, more suited for soil description, could be introduced.
- Several studies have been done with mixed sandy and clayey soil samples, but very few have been done with clay soils only. In this case there are some difficulties to model its behavior and a multi-pole Debye's equation and a new model suited for clay is needed.
- A new probe could be designed, in order first to obtain the majority of measurements falling in the low attenuation region (thus $\xi < 5$) and, second, to make it easier inserting soil samples into the probe. Worthless to remark that a new probe would require that the model has to be adapted to it and new parameters would rise.
- Water content is determined by means of experimental relations based on the knowledge of the low-frequency permittivity only (Topp et al., 1980). The model and its properties here introduced should be further investigated to gain a deeper insight in the relationship between model parameters and water content.

8. Acknowledgment

This study was partially funded by the Italian Ministry of Research through project PRIN2007-SSB3WP, "Experimental measurement of atmosphere-vegetation-soil interaction processes and numerical models of its response to climate change".

9. References

- Canone, D., M. Previati, S. Ferraris, M. P. & Haverkamp, R. (2009). A new coaxial time domain reflectometry probe for water content measurement in forest floor litter, *Vadose Zone J.*, 8(2): 363–372.
- Courtney, C. (1998). Time domain measurements of electromagnetic properties of materials, *IEEE Transactions on Microwave Theory and Techniques*, 46(5): 517–522.
- Evelt, S. & Parkin, G. (2005). Advances in soil water content sensing: the continuing maturation of technology and theory, *Vadose Zone J.* 4: 986–991.
- Evelt, S., Tolk, J. & Howell, T. (2005). Time domain reflectometry laboratory calibration in travel time, bulk electrical conductivity, and effective frequency, *Vadose Zone J.* 4: 1020–1029.
- Evelt, S., Tolk, J. & Howell, T. (2006). Soil profile water content determination: Sensor accuracy, axial response, calibration, temperature dependence, and precision, *Vadose Zone J.* 5: 894–907.
- Feng, W., Lin, C., Deschamps, R. & Drnevich, V. P. (1999). Theoretical model of multisection tdr measurement system, *Water Resour. Res.* 35: 2321–2331.

- Hansson, K. & Lundin, L.-C. (2006). Water content reflectometer application to construction materials and its relation to time domain reflectometry, *Vadose Zone J.* 5: 459-468.
- Hasted, J. (1973). *Aqueous Dielectric*, Chapman and Hall, London.
- Heimovaara, T. (1994). Frequency domain analysis of time domain reflectometry waveforms 1. measurements of the complex dielectric permittivity of soil, *Water Resour. Res.* 30: 189-199.
- Huisman, J., Bouten, W., Vrugt, J. & Ferré, P. (2004). Accuracy of frequency domain analysis scenarios for the determination of complex dielectric permittivity, *Water Resour. Res.* 40.
- Lide, D. (1992). *Handbook of chemistry and physics*, 73rd ed. CRC Press, London.
- Lin, C.-P. (2003). Analysis of nonuniform and dispersive time domain reflectometry measurement systems with application to the dielectric spectroscopy of soils, *Water Resour. Res.* 39: 6-11.
- Nozaki, R. & Bose, T. (1990). Broadband complex permittivity measurements by time-domain spectroscopy, *IEEE Trans. on Instr. and Meas.* 39: 945-951.
- Oswald, B., Doetsch, J. & Roth, K. (2006). A new computational techniques for processing transmission-line measurements to determine dispersive dielectric properties, *Geophysics* 71: k31-k35.
- Pozar, D. (2005). *Microwave engineering*, 3rd ed., John Wiley Sons, Inc., USA.
- Rautio, J. (1991). A de-embedding algorithm for electromagnetics, *Int. J. of Microwave and Millimeter-wave Computed-aided Engineering* 1: 282-287.
- Robinson, D., Jones, S., Wraith, J., Or, D. & Friedman, S. (2003). A review of advances in dielectric and electrical conductivity measurement in soils using time domain reflectometry, special section - advances in measurement and monitoring, *Vadose Zone J.* 2: 444-475.
- Robinson, D., Schaap, M., Or, D. & Jones, S. (2005). On the effective measurement frequency of time domain reflectometry in dispersive and nonconductive dielectric materials, *Water Resour. Res.* 41: 1-9.
- Roth, K., Schulin, R., Hler, H. F. & Attinger, W. (1990). Calibration of time domain reflectometry for water content measurement using a composite dielectric approach, *Water Resour. Res.* 10: 2267-2273.
- Savi, P., Maio, I. & Ferraris, S. (2010). The role of probe attenuation in the TDR characterization of dielectrics, *Electromagnetics* 30:6, 554-564.
- Somlo, P. & Hollway, D. (1969). Microwave locating reflectometer, *Electron. Lett.*, 5: 468-469.
- Topp, G., Davis, J. & Annan, P. (1980). Electromagnetic determination of soil water content: Measurements in coaxial transmission lines, *Water Resour. Res.* 16: 574-582.
- Topp, G. & Ferré, P.-A. (2002). *Water content, in Method of soil analysis, Part 4, Physical methods*, SSSA Book, vol.5 ed. J.H. Dane and G.C. Topp, Soil Sci. Soc. of Am., 417-446, Madison, Wis.
- Tripathi, V. & Jong, J. (1992). Time-domain characterization of interconnect discontinuities in high speed circuits, *IEEE Transactions on Components, Hybrids and Manufacturing Technology* 15(4): 497-504.
- Weerts, A., Huisman, J. & Bouten, W. (2001). Information content of time domain reflectometry waveforms, *Water Resour. Res.* 37: 1291-1299.